LA-UR- 08-7847

Approved for public release; distribution is unlimited.

Title:	Combinatorial nuclear level-density model
Author(s):	Sven Aberg and Henrik Uhrenholt, Lund University Peter Moller, T-2 Takatoshi Ichikawa, RIKEN
Intended for:	Physical Review C

Los Alamos
NATIONAL LABORATORY
EST. 1943

Form 836 (7/06)

Combinatorial nuclear level-density model

H. Uhrenholt[1], S. Åberg[1], P. Möller[2], T. Ichikawa[3]
[1] *Division of Mathematical Physics, LTH, Lund University, P.O. Box 118, S-221 00 Lund, Sweden*
[2] *Theoretical Division, Los Alamos National Laboratory, Los Alamos, NM 87545, USA*
[3] *RIKEN Nishina Center, RIKEN, Wako, Saitama 351-0198, Japan*

A microscopic nuclear level-density model is presented. The model is a completely combinatorial (micro-canonical) model based on the folded-Yukawa single-particle potential and includes explicit treatment of pairing, rotational and vibrational states. The microscopic character of all states enables extraction of level distribution functions with respect to pairing gaps, parity and angular momentum. The results of the model are compared to available experimental data: neutron separation energy level spacings, data on total level-density functions from the Oslo method and data on parity ratios.

I. INTRODUCTION

Nuclear many-body level-density models are key ingredients in nuclear reaction theories, where they, for example, govern the rates and decay patterns of astrophysical processes and nuclear fission. In statistical methods, for example the Hauser-Feshbach formalism [1], for describing nuclear reactions, a knowledge of the level density is crucial [2–4]. How to calculate the nuclear level density (NLD) has been a long-standing challenge that recently has been subject to renewed interest, theoretically as well as experimentally [5–8].

The simplest type of model is the Fermi-gas model, which is based on the partition-function method. It provides simple analytical formulas for the NLD [9]. Several phenomenological extensions have been proposed in order to reproduce experimental data. By adjusting free model parameters to data these models give unprecedented accuracy in the region of the parameter fit [4, 10]. Also semi-classical methods have been used to obtain expressions for the level density [11]. However, the Fermi-gas models are unreliable outside these regions, eg. when they are extrapolated to higher excitation energies or to nucleon numbers far from stability. Ideally nuclear structure should be included in NLD models. Several combinatorial models based on nuclear mean-field theory have been proposed, see eg. Refs. [12, 13]. Beyond mean-field methods have also been used to model the NLD, eg. the Shell-Model Monte-Carlo method [14, 15] and the interacting shell model [16]. These models take into account effective nucleon-nucleon interactions, but at the same time suffer from limitations due to the limited size of the Hilbert space and hence are presently unable to provide global predictions for level spacings at the neutron-separation energy.

Experimentally the NLD has been subject to renewed interest in the last decade partly due to the development of the Oslo method, which has provided a new types experimental data [17]. The Oslo method provides the level density over extended regions of excitation energy as opposed to the neutron-separation level-spacings data which only provide one data point at relatively high excitation energy. Also recent measurements of separate level densities of 2^+ and 2^- states [18] challenge theory to reproduce these observed parity ratios.

Few nuclear-structure models have been used to simultaneously globally describe nuclear masses, fission barriers, ground-state spins and decay rates. The microscopic-macroscopic FRLDM model has previously been used to model these observables [3, 19–21] and here serve as the starting point for calculating the nuclear level density. In this paper a combinatorial (micro-canonical) nuclear level-density model based on the folded-Yukawa single-particle model is presented. The model is fully microscopic with pairing correlations, vibrations, and rotational excitations calculated for each many-particle-many-hole excited state. No additional parameters are introduced, and no refitting of parameters of the FRLDM is performed. In Sec. II the combinatorial folded-Yukawa (CFY) level-density model is described. The model allows explicit tracking of quantum numbers, parity, angular momentum, pairing gaps of individual many-body configurations, and level distributions, which are discussed in Sec. III. Results from the CFY model are compared to experimental data in Sec. IV and in Sec. V the CFY model is compared to other theoretical NLD models. Finally, a short summary is given in Sec. VI.

II. THE COMBINATORIAL MODEL OF NLD (CFY)

It is important to base the level-density calculation on a mean field that is able to describe several nuclear physics properties. Therefore we base the CFY model on the folded-Yukawa single-particle potential with parameters, including ground-state deformations, taken from an extensive calculation of nuclear masses [19]. The NLD is calculated by means of combinatorial counting of excited many-particle-many-hole states. Pairing is taken into account for all excited states by explicitly solving the BCS equations for all individual configurations. Rotations are taken into account combinatorially with a pairing-dependent moment of inertia. The vibrational contribution to the NLD is investigated by including microscopically described phonons using the Quasi-particle Tamm-

Dancoff Approximation (QTDA). All produced nuclear levels are sorted into a binned level density, where the typical bin size is in the range 30–50 keV. The level density is calculated as

$$\rho(E_i, I, \pi) = \frac{1}{\Delta E} \int_{E_i - \frac{\Delta E}{2}}^{E_i + \frac{\Delta E}{2}} \sum_{\mu} \delta(E - E_\mu(I,\pi)) dE, \quad (1)$$

where E_i is the energy center of bin i and $E_\mu(I,\pi)$ denotes the calculated state with energy E_μ, angular momentum I and parity π. The total level density at a given excitation energy E is

$$\rho_{\rm tot}(E) = \sum_{I,\pi} \rho(E, I, \pi). \quad (2)$$

Deformed nuclei are assumed to have constant deformation for all excitation energies which is expected to be a good approximation for excitation energies below the neutron separation energy.

The good agreement between ground-state spins calculated in the FRLDM model and experiment implies that the single-particle spectrum close to the Fermi surface is well described [20]. The NLD critically relies on a good description of the single-particle structure and of low-lying excited states.

A. Pairing

The many-body wave-function of the excited states is approximated by the BCS wave-function with excited quasi-particles

$$|\tau\rangle = \prod_{\nu'' \in \tau_2} (-V_{\nu''} + U_{\nu''} a^\dagger_{\nu''} a^\dagger_{\bar{\nu}''}) \times \\ \times \prod_{\nu' \in \tau_1} a^\dagger_{\nu'} \prod_{\nu \in \tau_0} (U_\nu + V_\nu a^\dagger_\nu a^\dagger_{\bar{\nu}}) |0\rangle, \quad (3)$$

where τ_2, τ_1 and τ_0 denote the spaces of double, single and zero quasi-particle excitations, respectively. U_ν and V_ν are the standard BCS vacancy and occupation factors and $|0\rangle$ is the particle vacuum [22]. For the excited pairs in the group τ_2 the effect is simply

$$U_\nu \to -V_\nu, \qquad V_\nu \to U_\nu. \quad (4)$$

The pairing gap Δ and the Fermi energy λ are obtained by solving the BCS-equations

$$\Delta = G \left[\sum_{\nu \in \tau_0} U_\nu V_\nu - \sum_{\nu'' \in \tau_2} U_{\nu''} V_{\nu''} \right], \quad (5)$$

$$N = 2 \sum_{\nu \in \tau_0} V_\nu^2 + \sum_{\nu' \in \tau_1} 1 + 2 \sum_{\nu'' \in \tau_2} U_{\nu''}^2. \quad (6)$$

The theoretical BCS ground-state pairing gaps have been fitted to reproduce experimental nuclear masses [23]. This fit results in a 4.5 MeV average-pairing-gap parameter and a corresponding mass table with $\sigma = 0.63$ MeV using the BCS implementation of Ref. [24]. The pairing strength G, which is used for all excited states in the level-density calculation, is determined from this average pairing gap for each nuclear system, for details see Ref. [24].

It follows that the excitation energy of the intrinsic many-body configurations for one nucleon type is

$$E^t_{\rm mb} = 2 \sum_{\nu \in \tau_0} e_\nu V_\nu^2 + \sum_{\nu' \in \tau_1} e_\nu + 2 \sum_{\nu'' \in \tau_2} e_\nu U_{\nu''}^2 - \\ G \sum_{\nu \in \tau_0} V_\nu^4 - \frac{G}{2} \sum_{\nu' \in \tau_1} 1 - G \sum_{\nu'' \in \tau_2} U_{\nu''}^4 - \frac{\Delta^2}{G} - E^t_0, \quad (7)$$

where t denotes protons or neutrons and E^t_0 is the proton or neutron part of the ground-state energy. The total intrinsic excitation energy is $E_{\rm mb} = E^{\rm p}_{\rm mb} + E^{\rm n}_{\rm mb}$.

B. Rotations

Rotational states are taken into account combinatorially by adding a modified rotor energy to each of the intrinsic band-heads for deformed nuclei (defined as nuclei with calculated deformation $|\varepsilon_2| \geq 0.05$). The rotational energy is given by

$$E_{\rm rot} = \frac{I(I+1) - K^2}{2\mathcal{J}_\perp(\varepsilon_2, \Delta_{\rm p}, \Delta_{\rm n})}, \quad (8)$$

where I is the nuclear spin, K is the spin projection on the symmetry axis of the intrinsic state upon which the rotational band is built and $\mathcal{J}_\perp(\varepsilon_2, \Delta_{\rm p}, \Delta_{\rm n})$ is the moment of inertia around an axis perpendicular to the symmetry axis. The moment of inertia is approximated by the rigid-body moment of inertia with deformation ε_2, modified by the calculated pairing gaps for the considered state, as given in Ref. [25]. Given the angular momentum projection K and parity π of the band-head the rotational band includes the following levels

$$I^\pi = \begin{cases} K^\pi, (K+1)^\pi, (K+2)^\pi, \ldots & \text{if } K \neq 0, \\ 0^+, 2^+, 4^+, \ldots & \text{if } K = 0^+, \\ 1^-, 3^-, 5^-, \ldots & \text{if } K = 0^-. \end{cases} \quad (9)$$

The Coriolis anti-pairing effect is neglected and no virtual crossings of rotational bands are taken into account. Thus, the pairing gap is assumed to be unchanged from the band-head pairing gap for all states in the rotational band.

Fig. 1 shows the rotational enhancement, $K_{\rm rot}$, for ^{162}Dy (cf. Fig. 14) calculated as the ratio of the level density when rotations are included or excluded. For low excitation energies there are large fluctuations which are artifacts of the low level density combined with the smoothing procedure of Sec. II D. For higher excitation energies ($\gtrsim 3$ MeV) the rotational enhancement is a

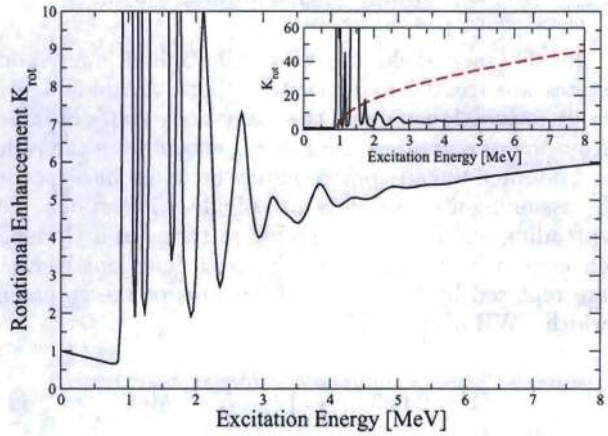

FIG. 1: (Color online) Rotational enhancement, $K_{\rm rot}$, for the nucleus ^{162}Dy as a function of excitation energy. The inset shows the enhancement compared to the simple enhancement model of Ref. [26] (red dashed line).

slowly increasing function, of the order of a factor 5. This prediction is in contrast to the SU(3) model of Ref. [26], which is often used to model NLD (see eg. Ref. [27]) and which is shown in the inset of Fig. 1. The SU(3) model gives almost an order of magnitude larger enhancement for excitation energies in the region of the neutron separation energy. Furthermore, there have been experimental efforts to search for the fade out of collective rotations at excitation energies far beyond the neutron separation energy, as given by the SU(3) model. These searches [28, 29] have given no experimental support for the fade-out profile used.

In the present model of combinatorially taking into account the rotations there is an explicit double counting of levels. However, this effect is expected to be negligible for excitation energies below the neutron separation energy [5].

C. Vibrations

In order to describe vibrational states the Quasiparticle-Tamm-Dancoff-Approximation (QTDA) is used. According to the Brink-Axel hypothesis [30, 31] phonons are built on every intrinsic many-body configuration $E_{\rm mb}$. The QTDA equation is solved for each state in order to get phonon excitation energies and wave-functions. The residual interaction is approximated by the double stretched Quadrupole-Quadrupole interaction. This interaction is well defined in the case of a harmonic oscillator potential. In the case of a finite-depth potential as the folded-Yukawa potential the interaction should take into account additional finite size effects, for example as is done in Ref. [32]. In the present work the finite-depth effects are ignored and the double stretched approach is used as defined in Refs. [33, 34].

The QTDA secular equation can be written [35]

$$\frac{1}{\chi_{2K}} = \sum_{\mu\nu} \frac{\left|\langle \mu \left| \bar{Q}_{2K} \right| \nu \rangle\right|^2 (U_\mu V_\nu + V_\mu U_\nu)^2}{(E^{\rm qp}_\mu + E^{\rm qp}_\nu) - \hbar\omega}, \qquad (10)$$

where the effect of Eq. (4) has not been explicitly written out. $\bar{Q}_{2K}$ is the double stretched quadrupole operator, where the components $K = 0$ and $K = 2$ are considered. The roots $\hbar\omega$ of this equation are the excitation energies of the vibrational phonons, whereas the poles $E^{\rm qp}_\mu = \sqrt{(e_\mu - \lambda)^2 + \Delta^2}$ are the unperturbed two-quasiparticle excitations on the many-body configuration $E_{\rm mb}$ and the e_μ are the single-particle energies.

The self-consistent coupling strength is given by [33]

$$\chi_{2K} = \frac{8\pi}{5} \frac{M\omega_0^2}{A\langle \bar{r}^2 \rangle + g_{2K}\sqrt{\frac{4\pi}{5}} A \langle \bar{Q}_{20} \rangle}, \qquad (11)$$

where $g_{20} = 1$ and $g_{22} = -1$. The expectation-values $\langle \bar{r}^2 \rangle$ and $\langle \bar{Q}_{20} \rangle$ are calculated in double stretched coordinates [33].

Double counting is explicitly avoided by the following procedure. The phonon wave functions are given by

$$\mathcal{O}^\dagger = \sum_{\mu,\nu} X_{\mu,\nu} a^\dagger_\mu a_\nu, \qquad (12)$$

where $X_{\mu,\nu}$ are the wave-function components of all excited quasi-particle states $a^\dagger_\mu a_\nu$ on top of the many-particle-many-hole configuration $E_{\rm mb}$. The level density is increased by one state at the energy of the phonon $\hbar\omega$, and decreased by the amount given by the wave-function component $X^2_{\mu,\nu}$ at the energy of the corresponding pole. The change in level density due to one phonon is thus

$$\delta\rho(E) = \delta(E - E_{\rm mb} - \hbar\omega) - \sum_{\mu,\nu} X^2_{\mu,\nu} \delta\left(E - E_{\rm mb} - (E^{\rm qp}_\mu + E^{\rm qp}_\nu)\right), \qquad (13)$$

where E is the excitation energy relative to the ground-state.

The vibrational enhancement factor in this method is in general quite small, of the order of a few percent. This is in sharp contrast to other methods that describe the vibrational enhancement in level densities. For example, the often employed attenuated phonon method gives up to an order of magnitude enhancement at the neutron separation energy [10, 12, 36]. Fig. 2 shows the vibrational enhancement as a function of excitation energy for ^{162}Dy. The effect is very small, close to 1 % at 7 MeV excitation energy. For the same nucleus the attenuated phonon method gives an enhancement factor of about 3 as shown in the inset of Fig. 2.

In calculations for a large number of nuclei it is possible to extract systematics of the Giant Quadrupole Resonances (GQR) and test if the double stretched quadrupole interaction is reasonable. Fig. 3 shows the

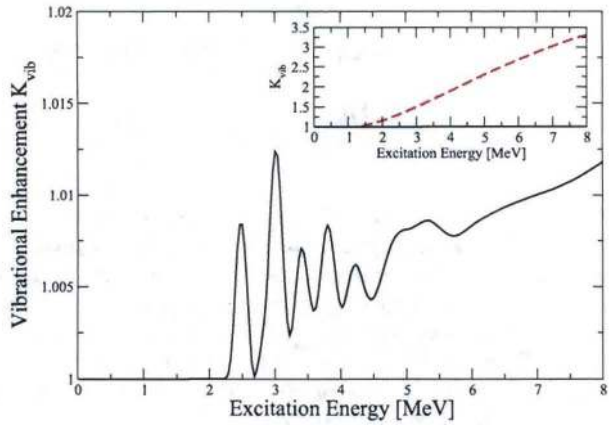

FIG. 2: (Color online) Vibrational enhancement, $K_{\rm vib}$, using the QTDA method for the nucleus ^{162}Dy as a function of excitation energy. The inset shows the enhancement compared to the enhancement of the attenuated phonon model of Ref. [10] (red dashed line).

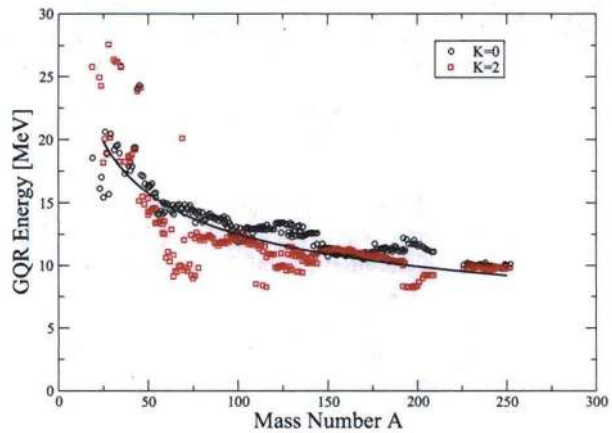

FIG. 3: (Color online) Energy of the giant quadrupole resonances as a function of mass number A. The black circles and red squares show the $K = 0$ and $K = 2$ resonances, respectively, and the solid black line shows the theoretical energy centroid $\omega_{\rm GQR} = 58A^{-1/3}$ [33].

energies of the $K = 0$ and $K = 2$ components of the (isoscalar) GQR as functions of mass number for the dataset of nuclei which are used to calculate the neutron resonance level spacings in Sec. IV A. The calculated GQR energies agree well with the systematic $\omega_{\rm GQR} = 58A^{-1/3}$ [33].

The level-density enhancement due to quadrupole vibrations is found to be very small. Higher multipole vibrations (as octupole vibrations) are expected to contribute with enhancements of the same order of magnitude or less and are neglected in the CFY model.

D. Many-body damping width

In the mean-field approach all excited many-body states are treated as non-interacting. A residual two-body interaction will mix the many-body states obtained from the combinatorics. Smearing effects from the residual interaction can approximately be taken into account by assuming a spreading width of all excited states. The spreading width is implemented in terms of a Gaussian envelope with width σ, i.e. the delta functions in Eq. 1 are replaced by Gaussians. Estimates of the spreading width FWHM gives [37]

$$\Gamma = 0.039 \left(\frac{A}{160}\right)^{-1/2} U^{3/2} \text{ MeV}, \qquad (14)$$

where the FWHM is related to the Gaussian spreading width $\sigma = \frac{\Gamma}{2\sqrt{2\ln 2}}$.

Assuming that all excited many-body states in an energy bin ΔE is uniformly distributed the level density are

$$\rho(E_i) = \sum_j \rho(E_j) \frac{1}{2} \left[\text{erf}\left(\frac{E_j + \Delta E/2 - E_i}{\sqrt{2}\sigma}\right) - \right.$$
$$\left. - \text{erf}\left(\frac{E_j - \Delta E/2 - E_i}{\sqrt{2}\sigma}\right)\right], \qquad (15)$$

for bin-point i. The method implies a smearing out of level-density properties over a range Γ, which is smoothly increasing with excitation energy. As a consequence fluctuations of energies and wave-functions in the range Γ follow GOE statistics of Random Matrix theory, that is often denoted as quantum chaos in the nucleus.

III. LEVEL DISTRIBUTIONS

In the present combinatorial approach it is possible to extract distributions of several quantities that depend on level densities.. We present here microscopically calculated distributions for pairing gaps, parity, and angular momentum.

A. Pairing-gap distribution

The BCS equations, Eqs. (5) and (6), are solved for all individual many-body configurations and hence pairing gaps for all states are obtained.

In Fig. 4 the distribution of proton pairing gaps for ^{162}Dy is shown for a number of excitation energies. For the lowest excitation energies only the ground-state and the states in the ground-state rotational band exist. The pairing gap of the levels in the rotational band is fixed to be the same as the pairing gap of the band-head, see Sec. II B. As the excitation energy increases levels with reduced pairing gaps appear. However, no transition to a

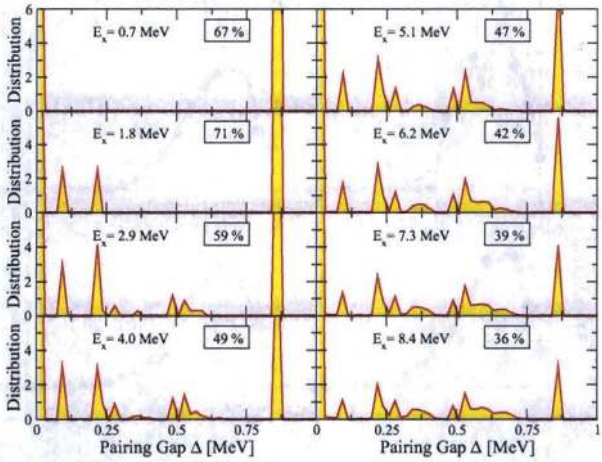

FIG. 4: (Color online) Proton pairing-gap distributions at different excitation energies E_x for ^{162}Dy shown in 20 keV pairing-gap bins. The proportion of paired states ($\Delta > 0$) are shown in percent in the boxes.

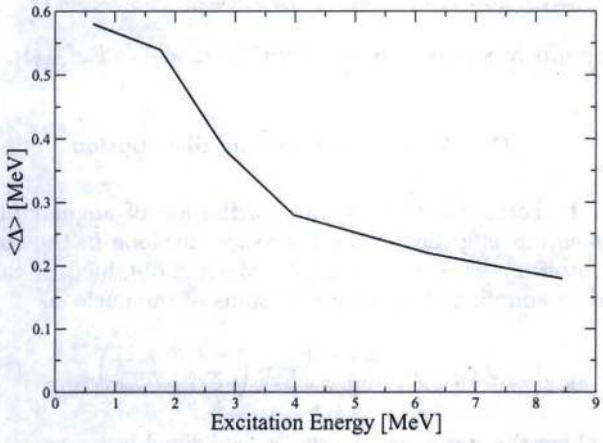

FIG. 5: Proton pairing gap mean value $\langle\Delta\rangle$ at different excitation energies for ^{162}Dy. The mean values are given by the distributions in Fig. 4.

completely unpaired system is observed, and levels with non-collapsed gaps ($\Delta > 0$) survive to the highest considered excitation energies. In the region of the neutron separation energy at 8.4 MeV 36% of the levels still have a non-zero pairing gap for ^{162}Dy, see Fig. 4. The mean value of the proton pairing gap $\langle\Delta\rangle$ at different excitation energies is shown in Fig. 5 for ^{162}Dy. Between 2 MeV and 3.5 MeV excitation energy there is a rapid decrease in the mean pairing gap. At higher excitation energies the decrease is slower. At 8.4 MeV excitation energy the mean value is $\langle\Delta\rangle = 0.2$ MeV. The non-collapsed pairing gaps influence the moment of inertia and keep it reduced as compared to the rigid-body value. This implies that even at excitation energies in the region of the neutron separation energy the moment of inertia is on average smaller than the rigid-body value.

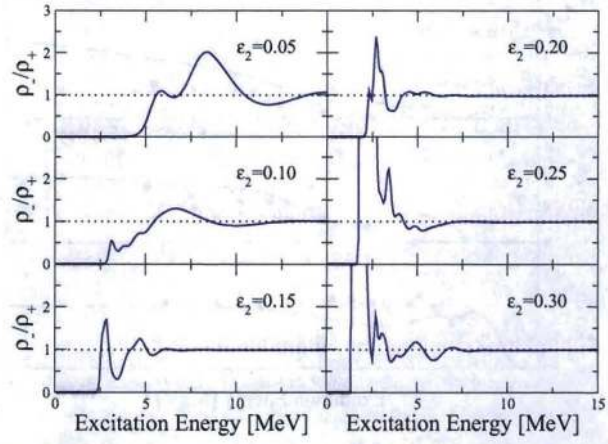

FIG. 6: (Color online) Parity ratio versus excitation energy for ^{84}Sr calculated with different ground-state deformations. Large deformations imply a parity distribution close to 1 even at low excitation energies. For small deformations the parity non-equilibrium can survive to high excitation energies.

B. Parity distribution

In Fermi-gas level-density models there is an implicit assumption of equal number of states with different parity at any given excitation energy. However, models that take into account microscopic effects show clear structure in the parity ratio, see eg. Refs. [14, 38, 39]. In connection with astrophysical reaction rates the parity ratio can be included in the Hauser Feshbach formalism, see eg Refs. [40, 41].

From the single-particle point of view it is clear that the parity ratio should show structure. For $^{84}_{38}Sr_{46}$ the situation is illuminating. The nucleus is close to spherical in its ground-state ($\varepsilon_2 = 0.05$) [19]. It has 10 protons in the pf shell and 6 neutrons in the $g_{9/2}$ shell. Since there are large gaps in the single-particle spectrum the energy to excite nucleons across the gaps, which cause changes in parity, is quite large. The parity ratio displays long-range oscillations (see upper left panel of Fig. 6) which are directly connected to the large single-particle gaps. The single-particle gaps effectively decrease with increasing deformation, and smaller oscillations are therefore expected at larger deformations. To test these ideas the parity ratio in ^{84}Sr is calculated at different deformations, see Fig. 6. Indeed, for larger deformations the oscillatory pattern vanishes and the parity ratio equilibrates at lower energies.

In Fig. 7 the parity ratios for ^{56}Fe, ^{60}Ni and ^{68}Zn are shown and compared to two calculations of Ref. [14]. The solid blue lines show the CFY model, the red dashed lines show the statistical parity projection model and the black dots show calculations using the Shell-Model Monte-Carlo method. The Fe and Ni isotopes are not equilibrated below 15 MeV in any of the calculations while ^{68}Zn equilibrates at much lower energies (below 10 MeV). For ^{60}Ni and ^{68}Zn there is a clear oscillatory

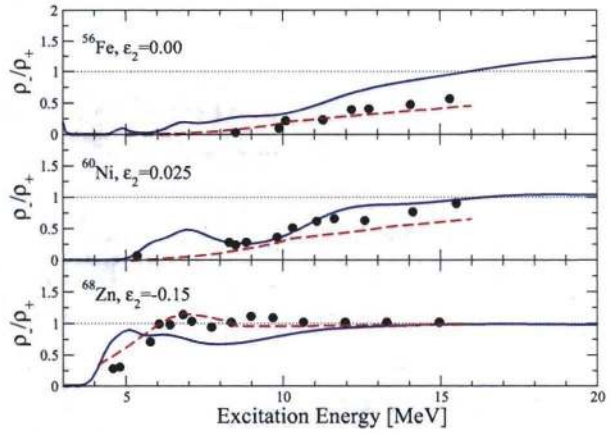

FIG. 7: (Color online) Parity ratio versus excitation energy. The solid blue lines are calculated with the CFY model. The red dashed line and blacked dots are given by a statistical model and a Monte-Carlo method, respectively [14].

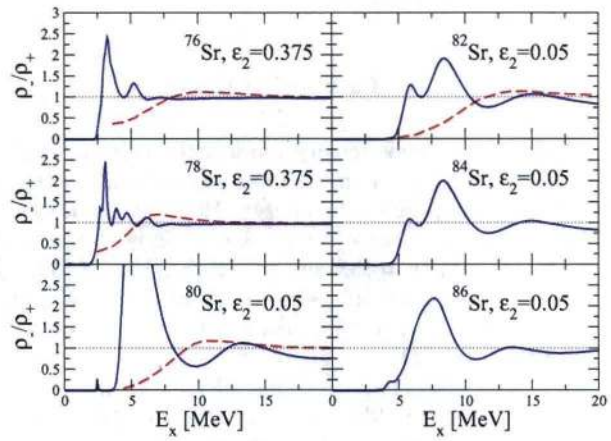

FIG. 8: (Color online) Parity ratio versus excitation energy for Sr isotopes. The solid blue lines are obtained from the CFY model and the dashed red lines are obtained from the statistical parity projection of Ref. [41].

behavior prior to equilibration in the CFY model, and in the case of Ni there is a good agreement between the Monte-Carlo method and the CFY model, especially in the region of 8–12 MeV excitation energy. Note, however, that fluctuations seen in the micro-canonical approach may be smeared out by the grand-canonical approach in Ref. [41]

The parity ratio has been calculated for Sr-isotopes within a statistical method in Ref. [41] where the impact on astrophysical reaction rates was investigated and found to be small. The statistical method gives at most one oscillatory maximum before it equilibrates, as seen in Fig. 8. In the CFY model the parity ratio has substantially more structure. Nuclei with small ground-state deformations show long range oscillations which survive to high excitation energies before equilibration. The overall

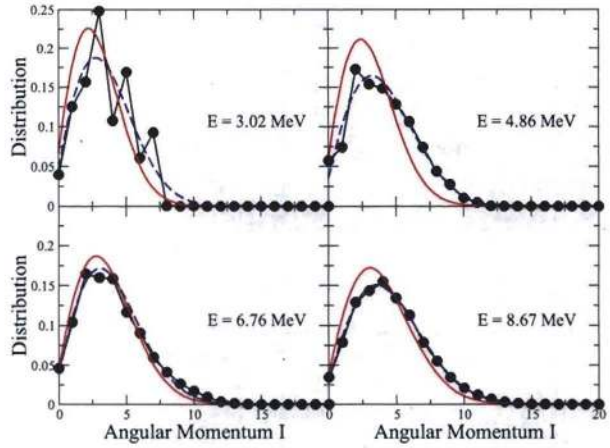

FIG. 9: (Color online) Angular-momentum distribution for ^{68}Zn in 4 different excitation-energy regions. The black lines with dots show results from the CFY model. The red solid lines and blue dashed lines show the Gaussians given by Eq. (16) using the spin cutoff factors from Ref. [4] and a direct fit to CFY, respectively.

results are quite different from the model of Ref. [41].

C. Angular momentum distribution

In Fermi-gas models the distribution of angular momentum is given by the Gaussian envelope in the spin cutoff model, see eg. Ref. [4], which is obtained by random coupling of uncorrelated spins of the nucleons

$$\mathcal{F}(U,J) = \frac{2J+1}{2\sigma^2}\exp\left(\frac{-J(J+1)}{2\sigma^2}\right), \qquad (16)$$

where the spin cutoff factor, σ, is defined by

$$\sigma^2 = \frac{\mathcal{J}_{\rm rigid}}{\hbar^2}\sqrt{\frac{U}{a}}, \qquad (17)$$

where $\mathcal{J}_{\rm rigid}$ is the rigid-body moment of inertia, $U = E - \delta$ is the effective excitation energy shifted by the back-shift δ, and a is the level-density parameter.

In Figs. 9 and 10 the angular-momentum distributions for ^{68}Zn and ^{162}Dy are shown for several excitation-energy regions. The black lines with dots show the CFY model results while the red solid lines show the Gaussian distribution of Eq. (16) with spin cutoff factors given in Ref. [4], and the blue dashed lines show Gaussian distributions fitted to the combinatorial calculation. For low excitation energies there are clear deviations from the Gaussian profiles while for higher excitations the combinatorial distribution tends to the Gaussian profile. In addition, for low excitation energies in ^{68}Zn there is an odd-even spin staggering which is not explained by the spin cutoff model. This effect has also been observed in Fe-isotopes in the Shell Model Monte-Carlo Method [15].

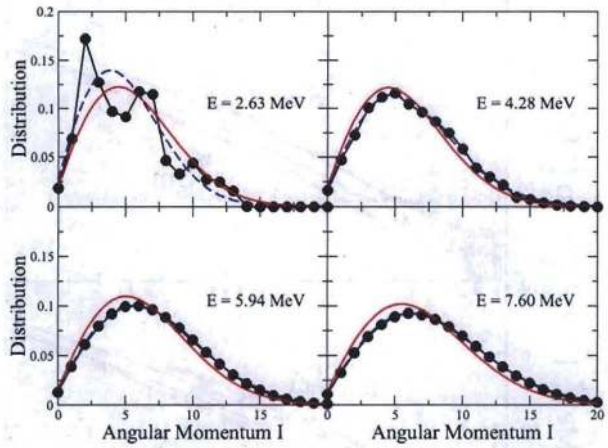

FIG. 10: (Color online) Similar to Fig. 9 but for ^{162}Dy.

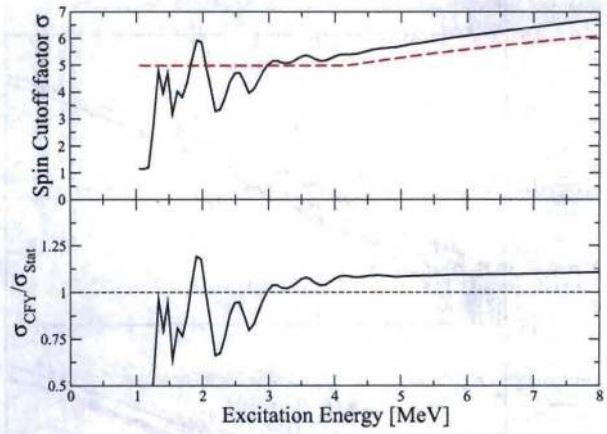

FIG. 11: (Color online) Top panel shows the spin cutoff factor as a function of excitation energy for ^{162}Dy in the CFY model (black solid line) and the statistical model of Ref. [4] (red dashed line). The bottom panel shows the ratio of the combinatorial and statistical spin cutoff factors of the top panel.

Fig. 11 shows the spin cutoff factor deduced from the CFY model (black solid line) and from the statistical model [4] (red dashed line), as a function of excitation energy for ^{162}Dy. The spin cutoff factor for excitation energies $\gtrsim 3$ MeV is similar in shape but $\sim$10 % larger than in the statistical model [4].

IV. COMPARISON WITH EXPERIMENTAL DATA

A. Neutron separation-energy level spacings

The s-wave neutron resonance spacings constitute the most comprehensive experimental database for comparison with NLD calculations [42]. This database serves as a benchmark for all large-scale level-density models

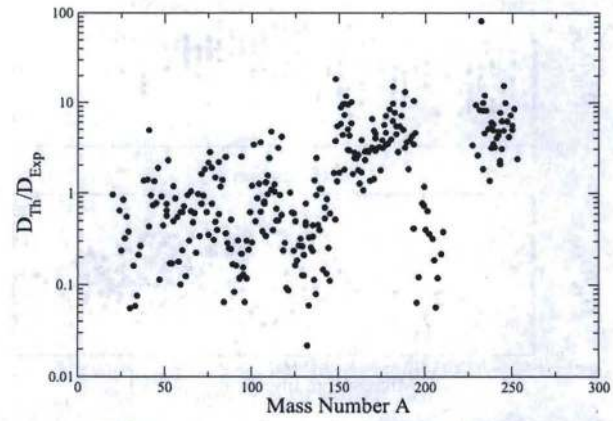

FIG. 12: Ratio between theoretical and experimental level spacings at neutron separation energy versus mass number A. The rms-factor is $f_{\rm rms} = 4.18$. The experimental data are taken from Ref. [42].

[4, 12, 13, 27].

The s-wave neutron resonance spacing D_0 at the neutron separation energy $S_{\rm n}$ of the compound nucleus (Z, N) is calculated as

$$\frac{1}{D_0} = \begin{cases} \rho(S_{\rm n}, I_0 + 1/2, \pi_0) + \rho(S_{\rm n}, I_0 - 1/2, \pi_0) & \text{for } I_0 > 0, \\ \rho(S_{\rm n}, 1/2, \pi_0) & \text{for } I_0 = 0. \end{cases} \quad (18)$$

where I_0 is the ground-state spin and π_0 is the ground-state parity of the target nucleus $(Z, N-1)$.

The quality of a model can be estimated by the rms-factor [13]

$$f_{\rm rms} = \exp\left[\frac{1}{N_e}\sum_{i=1}^{N_e} \ln^2 \frac{D^i_{\rm th}}{D^i_{\rm exp}}\right]^{1/2}, \quad (19)$$

and the mean factor

$$m = \exp\left[\frac{1}{N_e}\sum_{i=1}^{N_e} \ln \frac{D^i_{\rm th}}{D^i_{\rm exp}}\right], \quad (20)$$

where $D^i_{\rm th}$ and $D^i_{\rm exp}$ are the theoretical and experimental level spacings and N_e is the number of nuclei in the database. The CFY model gives $f_{\rm rms} = 4.18$, see Fig. 12, which is comparable to other statistical and combinatorial models, see Table. I. The mean factor is $m = 1.09$ which indicates that the model is describing the level spacings well on average.

As seen in Fig. 12 there seems to be a clear residual shell structure in the level spacings, especially in the doubly magic ^{208}Pb region. A similar effect can be observed for the Gogny model in Ref. [13] and in results of Skyrme-model calculations with the BSk9 interaction, as shown in Ref. [12]. The overall deviation from experimental

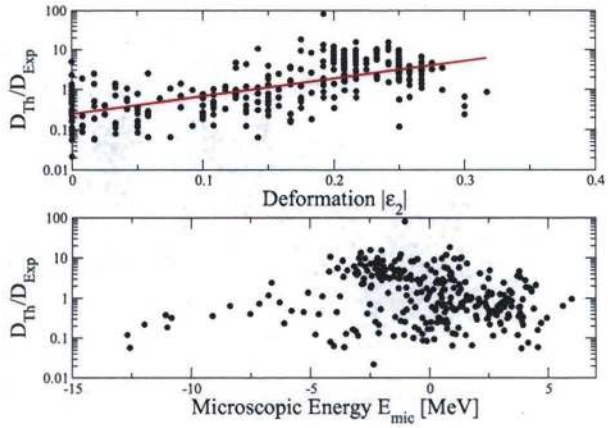

FIG. 13: (Color online) Top panel shows the ratio between theoretical and experimental level spacings at neutron separation energy versus the absolute value $|\varepsilon_2|$ of the calculated quadrupole deformation. The bottom panel shows this ratio as a function of the microscopic energy. The solid red line shows an exponential fit to illustrate the correlation. The microscopic energies and the quadrupole deformations are taken from Ref. [19]. The experimental data are from Ref. [42].

data is correlated with the ground-state deformation as seen in Fig. 13 where the level spacings are shown versus the absolute value of the deformation. However, there is no clear correlation with the microscopic energy $E_{\rm mic}$ of Ref. [19] as seen in the lower panel of Fig. 13.

B. Detailed level-density functions

The Oslo method is a commonly used experimental method for extracting detailed level-density functions for large ranges of excitation energy [17]. It provides a valuable test for NLD models, and below the CFY is compared to data for a number nuclei where experimental data are available [43–48].

In Fig. 14 we show level densities of the rare-earth nuclei ^{148,149}Sm, ^{161,162}Dy, ^{166,167}Er, and ^{170,171,172}Yb as functions of excitation energy. The data are in general well reproduced by the CFY model, with an error of less than a factor of 2. The good agreement between the calculated and experimental slopes slopes indicates that the single-particle structure and the moments of inertia in the rotational bands are sound. However, an observable trend in this mass region is that the level density for even-even nuclei is slightly over-estimated and for odd nuclei the level density is slightly under-estimated. The effective back-shift is to a large extent controlled by the ground-state pairing gap. By fine-tuning the pairing gaps it is possible to get an almost perfect agreement with experiment. However, in this paper no such local fits are performed. Instead the ground-state pairing gaps are given by the mass model, see the introduction..

Experimental level-density functions are available also

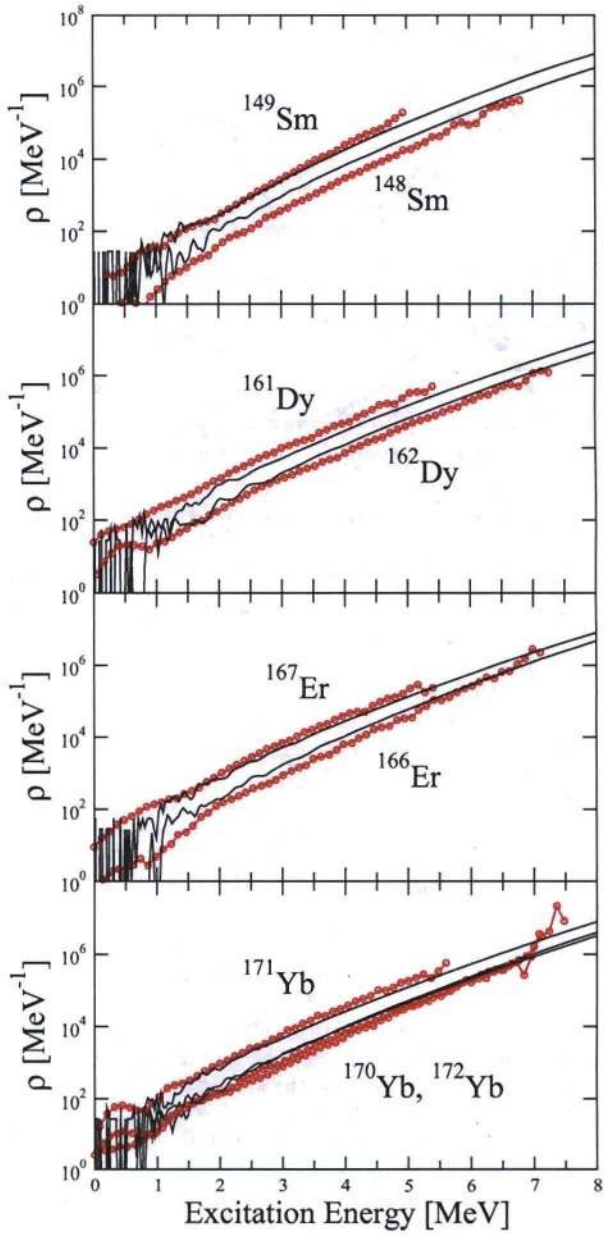

FIG. 14: (Color online) Level densities ρ as functions of excitation energy for Sm, Dy, Er and Yb isotopes. The black solid lines show the CFY model results and the red dots show the experimental data [45–48].

for lighter mass regions and in Figs. 15 and 16 data for V and Mo isotopes are shown. The overall agreement between the model and these experimental data is somewhat inferior to what was obtained in the rare-earth region. For the Mo isotopes in Fig. 16 the CFY model is roughly a factor of 3 too large for high excitation energies while for the V isotopes in Fig. 15 the over-estimation is roughly a factor of 4. However, these errors are consistent with the overall results from the neutron separation level spacing, see Fig. 12, which have an overall

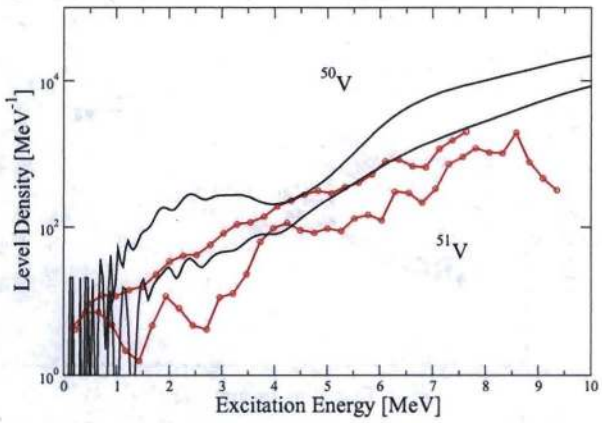

FIG. 15: (Color online) Level densities as functions of excitation energy for ^{50,51}V. The black solid lines show results from the combinatorial calculation and the red dots show the experimental data [43].

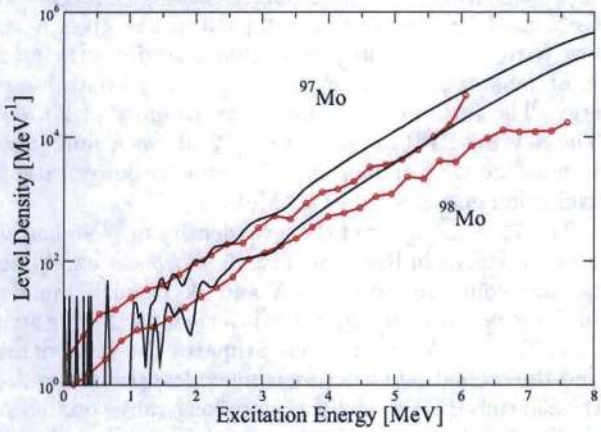

FIG. 16: (Color online) Level densities as functions of excitation energy for ^{97,98}Mo. The black solid lines show results from the combinatorial calculation and the red dots show the experimental data [44].

$f_{\rm rms} = 4.18$. Also, the slopes and the detailed structures are not as well described in these nuclei as in the rare-earths. Especially ^{50}V exhibit an oscillatory pattern in the CFY model, which is an effect of the small ground-state deformation $\varepsilon_2 = 0.05$. A corresponding oscillatory pattern is not as clearly present in the experimental data. In ^{51}V the features of the model results and experimental data are reversed. The experimental data shows oscillatory behavior while the CFY model is more smooth. The ground-state deformation is slightly larger with $\varepsilon_2 = 0.083$, which in the CFY model means that since the moment of inertia is larger the rotational states have a larger influence and smooths the level density.

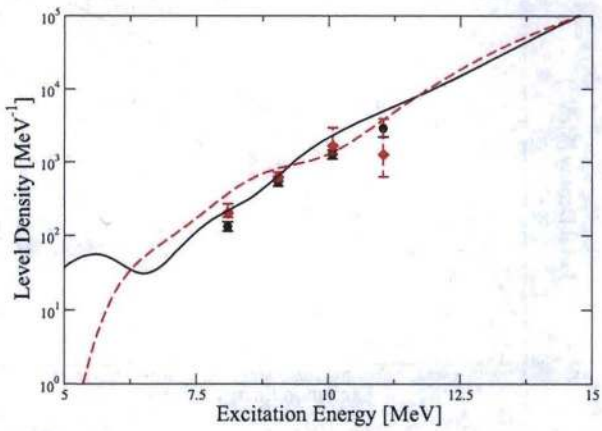

FIG. 17: (Color online) Level density of the 2^+ (black solid) and 2^- (red dashed) components of the level density as a function of excitation energy for ^{90}Zr. Data from Ref. [18] are shown as black dots and red diamonds with error-bars for 2^+ and 2^-, respectively.

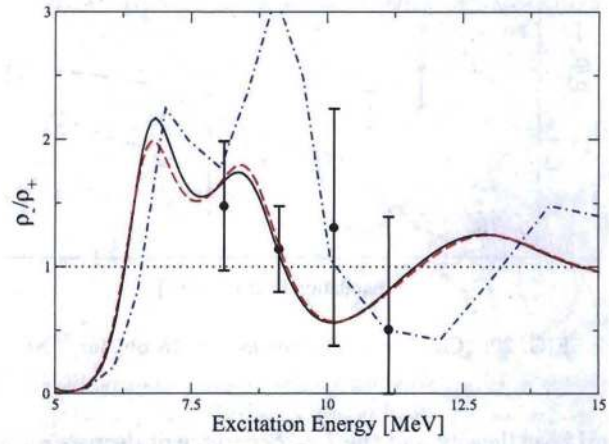

FIG. 18: (Color online) Parity ratio versus excitation energy for ^{90}Zr. The solid black and dashed red lines show the CFY model results for the total level density and the I=2 component, respectively. The blue dot-dashed line show the Skyrme-HFB model of Ref. [12]. Data are from Ref. [18].

C. Parity Ratio

The parity ratio has been measured experimentally by Kalmykov et.al. [18] for the two spherical nuclei, ^{58}Ni and ^{90}Zr. For these nuclei the $I = 2$ angular-momentum components of the level density are measured and separated into parity components. In Fig. 17 the level-density components $\rho(E, I = 2, \pi = \pm 1)$ for ^{90}Zr are compared to CFY model calculations. The level densities from the CFY model are in good agreement with experimental data, and in Fig. 18 the parity ratio is shown. Predictions for the total level density as well as the $I = 2$ component are shown as black solid and red dashed lines, respectively. The difference between the parity ratio for the to-

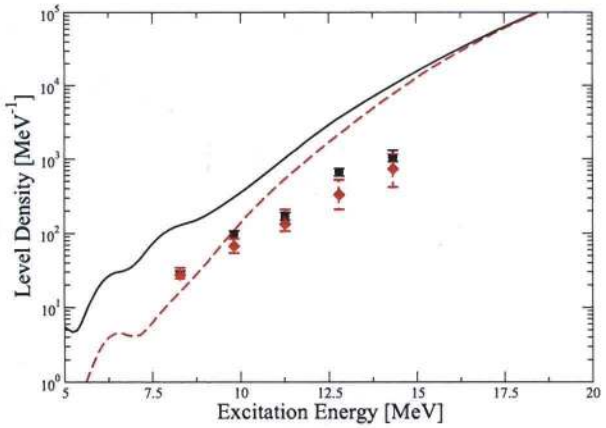

FIG. 19: (Color online) Same as Fig. 17 but for ^{58}Ni.

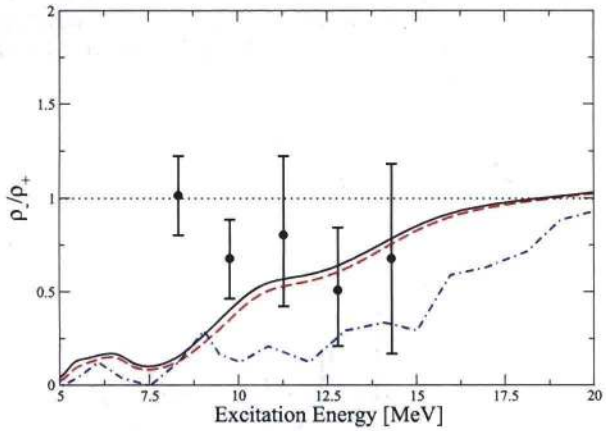

FIG. 20: (Color online) Same as Fig. 18 but for ^{58}Ni.

tal level density and the $I = 2$ component decreases with excitation energy, because the spin cutoff model becomes more realistic when the excitation energy increases, see Sec. III C. For the parity ratio the CFY model result is within the experimental error-bars for all excitation energies and seems to show a similar pattern as the experiments: a high parity ratio at 8 MeV and a low ratio at 11 MeV excitation energy. The blue dot-dashed line shows the Skyrme-HFB model of Ref. [12]. It is also within the experimental error-bars for all excitation energies except at 9 MeV where the HFB model gives a large positive ratio (~ 3) while the experiments and the CFY model are close to unity.

The $I = 2$ component of the level density in ^{58}Ni is shown in Fig. 19. The agreement between experimental data and the CFY model is somewhat inferior to what we obtained for ^{90}Zr. For both parities the level density seems to increase faster in the CFY model than what is seen in the experimental data. At 14 MeV excitation energy the model overestimates the level density by roughly a factor of 6. The parity ratio is shown in Fig. 20. The experimental parity ratio is close to unity at 8 MeV and

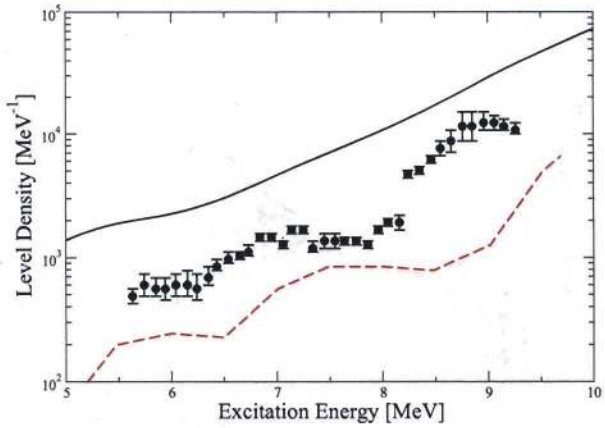

FIG. 21: (Color online) Level density of the 1^+ components of the level density as a function of excitation energy for ^{90}Nb. The black solid and red dashed lines show the CFY model and Skyrme-HFB model of Ref. [12], respectively. Data from Ref. [18] are shown as black dots with error-bars.

then decreases with increasing excitation energy. The CFY model shows a different pattern. It gives a very low parity ratio at low excitation energies with an almost monotonic increase with increasing excitation energy. The ratio only becomes close to unity at 20 MeV. The Skyrme-HFB model of Ref. [12] shows a similar pattern as the CFY model but with an even lower ratio for excitation energies below 20 MeV.

The 1^+ component of the level density of ^{90}Nb has also been measured in Ref. [18]. Fig. 21 shows the experimental data compared to the CFY and Skyrme HFB models. In the experimental data there is a clear oscillating structure. The CFY model over-estimates the level density and the oscillating structure is much less pronounced. In the Skyrme-HFB model there are long-range oscillations similar to what is seen in the experimental data, but the energy separation between consecutive minima is larger. The level density is under-estimated in the Skyrme-HFB model, whereas the CFY model over-estimates the level density by a similar factor.

V. COMPARISON WITH OTHER MODELS

The CFY model is here compared to other statistical and combinatorial NLD models that provide neutron resonance level spacings. In general the statistical models listed in in Table. I have an rms deviation just below 2. This low rms deviation is obtained because several parameters in the level-density formulas are directly adjusted to the neutron separation-energy level spacings and low-lying discrete energy levels.

The back-shifted Fermi model of Ref. [27] is based on a simple Fermi-gas formula whereas the Constant Temperature model is based on the approach of Gilbert and Cameron [8]. Both models contain explicit enhance-

Statistical Models	$f_{\rm rms}$	Ref.
Back-shifted Fermi Model	1.71	[27]
Const. Temp. Model	1.77	[27]
Back-shifted Fermi + Const. Temp. Model	1.7	[4]
Generalized Superfluid Model	1.94	[27]

Combinatorial Models	$f_{\rm rms}$	Ref.
Skyrme-HFB	2.35	[27]
Gogny-HFB	4.55	[13]
CFY	4.18	Present

TABLE I: Table of rms-factors $f_{\rm rms}$ for statistical and combinatorial models for neutron separation energy level spacings [4, 13, 27].

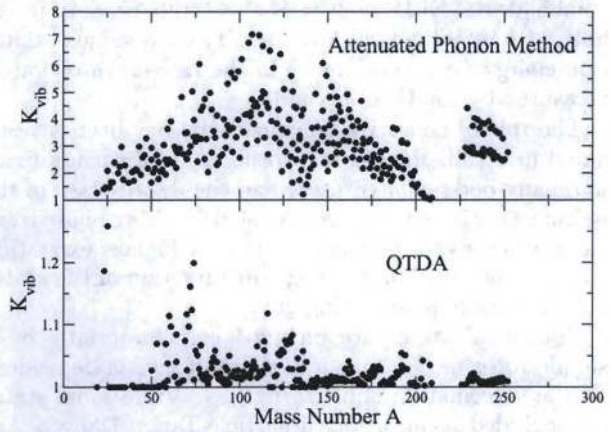

FIG. 22: Vibrational enhancements at the neutron separation energy in the attenuated phonon method (top panel) and the QTDA method (bottom panel) versus of mass number A.

ment factors for rotations and vibrations. The model by Rauscher, Thielemann and Kratz [4] is also based on the approach of Gilbert and Cameron. In contrast to the first two models this model has no explicit enhancement factors for rotations and vibrations. It accounts for shell effects and thermal damping in terms of an effective level-density parameter. The model uses the microscopic energy corrections of Ref. [19] together with three free parameters in the fitting procedure. The Generalized Superfluid Model is similar to the models mentioned above. In addition it takes into account how pairing evolves with increasing excitation energy. It also incorporates explicit rotational and vibrational enhancements [27].

Predictions by statistical models in regions outside the fitting region probably give much less accurate results than in the adjustment region. On the other hand, since the combinatorial models are all based on calculated single-particle spectra they could in principle have better predictive power, in particular in regions where the single-particle model is sound. In contrast, they are not equally flexible in terms of parameter fits to the level spacings database. Therefore, the rms deviation factor of combinatorial models with respect to known data is larger than for the statistical models. The $f_{\rm rms} = 4.18$ for the CFY model is about a factor of 2 larger than in statistical models. However, the latter result is obtained with *no* parameters specifically fitted to the level-density data. But it is impressive that the mean deviation factor $m = 1.09$ indicates that the level density is on average correct. There is no need to include any additional order of magnitude collective enhancements in the CFY model as proposed by the SU(3) rotational enhancement or the attenuated phonon method, see Figs. 1 and 2 and the discussion below.

In the lower part of Table. I the CFY model is compared to two other large-scale combinatorial NLD models based on the HFB method. The model of Ref. [13] is based on the Gogny D1S interaction for the mean-field and incorporates combinatorial rotations (similar to Sec. II B but no pairing dependence of the moment of inertia), and the attenuated phonon method is applied to account for vibrational states. Pairing is included explicitly for the ground-state, and excited states are back-shifted by an energy-dependent gap procedure. The model gives $f_{\rm rms} = 4.55$ for the subset of even-even axially deformed nuclei. The error is slightly larger than the CFY model.

For the Skyrme-HFB NLD model the deviation factor is $f_{\rm rms} = 2.35$ [27], which is $\sim 35\%$ larger than the statistical models and 44% smaller that in the CFY model. This model is based on a Skyrme-HFB mean-field together with combinatorial rotations and the attenuated phonon method for modeling vibrational states. In addition a phenomenological deformation change from deformed to spherical shape at some specified excitation energy is incorporated.

The attenuated phonon method is a phenomenological way to model nuclear vibrations, see eg. Refs. [10, 12]. It assumes that the quadrupole and octupole phonon states in nuclei can be modeled by a gas of non-interacting bosons. The vibrational excitation energies are taken from systematics of the lowest non-rotational 2^+ and 3^- states. The model is formulated as a multiplicative factor $K_{\rm vibr} = \exp\left[\delta S - \delta U/T\right]$ which enhances the level density. T is the nuclear temperature and the δS and δU are the entropy and internal energy change induced by the bosons. The occupation probabilities of the bosons are described by damped Bose statistics, where the damping sets in at considerably higher energies than the neutron separation energy. At excitation energies close to or below the neutron separation energy the damping has negligible effect which implies that the phonons are allowed to be repeated several times. The repetition of phonons effectively leads to a large enhancement. But, numerous repetitions of phonons is highly questionable even in strongly vibrational nuclei, see eg. Ref. [49].

The vibrational enhancement at the neutron separation energy is quite small in the QTDA method as compared to the attenuated phonon method, see Fig. 22. The

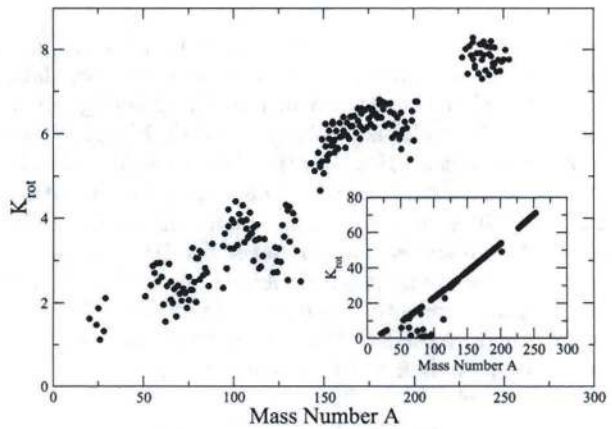

FIG. 23: Rotational enhancement at the neutron separation energy in the CFY model and in the SU(3) method of Ref. [26] (inset) versus mass number A.

QTDA gives an enhancement of the order of a few percent compared to up to a factor 7 in the attenuated phonon method. The QTDA phonons are microscopically built from states with energies not much different than the phonon energy. The way to fully account for double-counting of phonon states (Eq. 13), thus implies a small vibrational enhancement. On the other hand, phonons in the attenuated phonon model are not described microscopically, and double-counting of states may appear.

Inclusion of the attenuated phonon model in the CFY model would introduce a too large level density on average and thus a poorer total result in general with $f_{\rm rms} = 6.24$ and $m = 0.35$. That corresponds to a systematic over-estimate of the level density at the neutron separation energy by a factor of 3. The attenuated phonon method gives the largest vibrational contributions for medium-mass nuclei, especially in the $A = 100$ and $A = 150$ regions. There does not seem to be a substantial over-estimate of the level spacings (i.e. under-estimate of level density) in these regions in the CFY model as seen in Fig. 12. However, inclusion of the attenuated phonon method would give almost an order of magnitude over-estimate of the level density in these regions.

The QTDA gives its largest vibrational enhancements for the $A = 75$ region and Cd isotopes in the $A = 115$ region, see Fig. 22, which is consistent with the fact that Cd isotopes are known to have a strong vibrational character, see eg. Refs. [49, 50].

In Fig. 23 the rotational enhancement in the CFY model at the neutron separation energy is shown . The enhancement is increasing almost linearly with mass number. The inset shows the SU(3) rotational enhancement model which gives an order-of-magnitude larger enhancement compared to the CFY model. Hence, both phenomenological models, the SU(3) rotational enhancement and the attenuated phonon model, each gives almost an order-of-magnitude larger enhancement than what is obtained in the approach used in the CFY model. Since the neutron resonance level spacings are well described on average in the CFY model there is therefore no justification to use additional order-of-magnitude collective enhancement factors in the CFY model, although such factors occur in the SU(3) and attenuated phonon methods.

VI. SUMMARY

A combinatorial model for the nuclear level density is presented. The model is based on the folded-Yukawa single-particle model with ground-state deformations and parameters from Ref. [19]. The model is used to calculate the neutron resonance level spacings, yielding an rms deviation of $f_{\rm rms} = 4.18$, which is comparable to other combinatorial NLD models. It also compares very favorably with experimental level density data versus excitation energy for several nuclei in the rare-earth region as measured by the Oslo method.

The role of collective enhancements has been investigated in detail. Pairing is incorporated for each individual many-body configuration and the distribution of the pairing gaps is investigated. No sharp pairing phase transition is observed. Instead, even at the highest excitation energy considered, a non-negligible fraction of the states have a considerable pairing gap.

Rotational states are included combinatorially by a simple rotor model with a moment of inertia dependent on the deformation and pairing gap. Vibrational states are included using a Quasi-particle-Tamm-Dancoff Approximation. It is found that the vibrational enhancement in the QTDA model is very small, on the order of a few percent at the neutron separation energy. This model result is in sharp contrast to the widely used attenuated phonon model [10], which gives up to a factor of 7 enhancement at the neutron separation energy. Since the neutron separation level spacings are on average well described in the CFY model further inclusion of vibrational enhancements (like the attenuated phonon method) would introduce large mean discrepancies relative to the experiments, see Sec. IV A.

The parity distribution in the CFY model shows large oscillatory patterns for nuclei which have large gaps in the single-particle spectrum, separating shells with different parities. This is often the case for nuclei with small deformations. The patterns are quite different from the smooth pattern of the statistical parity distribution model of Ref. [14]. The CFY model is compared to other models and to experimental data when available.

The angular-momentum distribution in the CFY model is compared to the spin cutoff model in Sec. III C. It is found that the Gaussian envelope of the spin cutoff model is in good agreement with the CFY model for high excitation energies. For low excitation energies the CFY model shows some structure. For the nucleus ^{162}Dy the spin cutoff factor σ is compared in the CFY model with

the results of a commonly used formula. It is found that the spin cutoff factors in the two models are very similar in functional form but differ by $\sim 10\%$ at high excitation energies.

Acknowledgments

H. U. would like to acknowledge the hospitality of the Los Alamos National Laboratory during several visits. Discussions with T. Rauscher, F.-K. Thielemann, K.-L. Kratz, M. Guttormsen and A. Richter are acknowledged.

This work was supported by travel grants for P. M. to JUSTIPEN (Japan-U. S. Theory Institute for Physics with Exotic Nuclei) under grant number DE-FG02-06ER41407 (U. Tennessee).

This work was partially carried out under the auspices of the National Nuclear Security Administration of the U. S. Department of Energy at Los Alamos National Laboratory under Contract No. DE-AC52-06NA25396.

[1] W. Hauser and H. Feshbach, Phys. Rev. **87** (1952) 366
[2] T. Rauscher and F.-K. Thielemann, Atomic Data and Nuclear Data Tables, **75** (2000) 1
[3] P. Möller, *et. al.*, Submitted to Phys. Rev. **C**
[4] T. Rauscher, F.-K. Thielemann and K.-L. Kratz, Phys. Rev. **C 56** (1997) 1613
[5] S. Bjørnholm, A. Bohr and B. Mottelson, *Physics and Chemistry of Fission*, Proceedings of a Conference at Rochester (IAEA, Vienna), (1974) Vol. 1, p. 367
[6] A. Bohr and B. R. Mottelson, *Nuclear Structure, Volume II* (Benjamin, Reading, MA, 1975)
[7] V. G. Soloviev, Nucl. Phys. **69** (1965) 1
[8] A. Gilbert and A.G.W. Cameron, Can. J. Phys. **43** (1965) 1446
[9] A. Bohr and B. R. Mottelson, *Nuclear Structure, Volume I* (Benjamin, Reading, MA, 1969)
[10] A.V. Ignatyuk, J.L. Weil, S. Raman and S. Kahane, Phys. Rev. **C 47** (1993) 1504
[11] P. Leboeuf and J. Roccia, Phys. Rev. Lett. **97** (2006) 010401
[12] S. Hilaire and S. Goriely, Nucl. Phys. **A 779** (2006) 63
[13] S. Hilaire, J. P. Delaroche and M. Girod, Eur. Phys. J. **A 12** (2001) 169
[14] Y. Alhassid, G. F. Bertsch, S. Liu and H. Nakada, Phys. Rev. Lett. **84** (2000) 4313
[15] Y. Alhassid, S. Liu and H. Nakada, Phys. Rev. Lett. **99** (2007) 162504
[16] M. Horoi, J. Kaiser and V. Zelevinsky, Phys. Rev **C 67** (2003) 054309
[17] A.Schiller *et. al.*, Nucl. Instr. Meth. Phys. Res. **A 447** (2000) 498
[18] Y. Kalmykov *et.al.*, Phys. Rev. Lett. **99** (2007) 202502
[19] P. Möller, J. R. Nix, W. D. Myers and W. J. Swiatecki, Atomic Data and Nuclear Data Tables, **59** (1995) 185
[20] L. Bonneau, P. Quentin and P. Möller, Phys. Rev. **C 76** (2007) 024320
[21] P. Möller, J. R. Nix and K.-L. Kratz, Atomic Data and Nuclear Data Tables, **66** (1997) 131
[22] T. Døssing *et. al.*, Phys. Rev. Lett. **75** (1995) 1276
[23] P. Möller and J.R. Nix, Nucl. Phys. **A 536** (1992) 20
[24] H. Olofsson, R. Bengtsson and P. Möller, Nucl. Phys. **A 784** (2007) 104
[25] R. Bengtsson and S. Åberg, Phys. Lett. **B 172** (1986) 277
[26] G. Hansen and A. S. Jensen, Nucl. Phys. **A 406** (1983) 236
[27] A. J. Koning, S. Hilaire and S. Goriely, Nucl. Phys. **A 810** (2008) 13
[28] A. R. Junghans, Nucl. Phys. **A 629** (1998) 635
[29] S. Komarov *et. al.*, Phys. Rev. **C 75** (2007) 064611
[30] D. M. Brink, PhD-thesis (Oxford University, 1955)
[31] P. Axel, Phys. Rev. **126** (1962) 671
[32] V. O. Nesterenko, W. Kleinig, V. V. Gudkov and J. Kvasil, Phys. Rev. **C 53** (1996) 1632
[33] H. Sakamoto and T. Kishimoto, Nucl. Phys. **A 501** (1989) 205
[34] S. Åberg, Phys. Lett. **B 157** (1985) 9
[35] D. J. Rowe, *Nuclear Collective Motion - Models and Theory* (Butler & Tanner Ltd, Frome and London, 1970)
[36] A. V. Ignatyuk, *Statistical Properties of excited atomic nuclei* (Transl. from Russian) IAEA, INDC(CCP)-233(L), Vienna, IAEA 1985
[37] B. Lauritzen, T. Døssing and R. A. Broglia, Nucl. Phys. **A 457** (1986) 61
[38] S. M. Grimes, Phys. Rev. **C 38** (1988) 2362
[39] N. Cerf, Nucl. Phys. **A 554** (1993) 85
[40] H. P. Loens *et. al.*, Phys. Lett. **B 666** (2008) 395
[41] D. Mocelj *et. al.*, Phys. Rev. **C 75** (2007) 045805
[42] RIPL2, Reference Input Parameter Library, IAEA-Tecdoc, 2005, available at http://www-nds.iaea.or.at/ripl2.
[43] A. C. Larsen *et. al.*, Phys. Rev. **C 73** (2006) 064301
[44] R. Chankova *et. al.*, Phys. Rev. **C 73** (2006) 034311
[45] S. Siem *et. al.*, Phys. Rev. **C 65** (2002) 044318
[46] M. Guttormsen *et. al.*, Phys. Rev. **C 68** (2003) 064306
[47] E. Melby *et. al.*, Phys. Rev. **C 63** (2001) 044309
[48] A. Schiller *et. al.*, Phys. Rev. **C 63** (2001) 021306(R)
[49] P.E. Garrett, K.L. Green and J.L. Wood, Phys. Rev. **C 78** (2008) 044307
[50] J.L. Wood *et. al.*, Phys. Rep. **215** (1992) 101